

RESEARCH

Open Access



# Y-mediated optimization of 3DG-PbO<sub>2</sub> anode for electrochemical degradation of PFOS

Xiaoyue Duan<sup>1,2,3</sup>, Ziqi Ning<sup>2,3</sup>, Weiyi Wang<sup>1</sup>, Yitong Li<sup>2,3</sup>, Xuesong Zhao<sup>2,3</sup>, Liyue Liu<sup>3</sup>, Wenqian Li<sup>3</sup> and Limin Chang<sup>1\*</sup>

## Abstract

In our previous study, the three-dimensional graphene-modified PbO<sub>2</sub> (3DG-PbO<sub>2</sub>) anode was prepared for the effective degradation of perfluorooctanesulfonate (PFOS) by the electrochemical oxidation process. However, the mineralization efficiency of PFOS at the 3DG-PbO<sub>2</sub> anode still needs to be further improved due to the recalcitrance of PFOS. Thus, in this study, the yttrium (Y) was doped into the 3DG-PbO<sub>2</sub> film to further improve the electrochemical activity of the PbO<sub>2</sub> anode. To optimize the doping amount of Y, three Y and 3DG codoped PbO<sub>2</sub> anodes were fabricated with different Y<sup>3+</sup> concentrations of 5, 15, and 30 mM in the electroplating solution, which were named Y/3DG-PbO<sub>2</sub>-5, Y/3DG-PbO<sub>2</sub>-15 and Y/3DG-PbO<sub>2</sub>-30, respectively. The results of morphological, structural, and electrochemical characterization revealed that doping Y into the 3DG-PbO<sub>2</sub> anode further refined the  $\beta$ -PbO<sub>2</sub> crystals, increased the oxygen evolution overpotential and active sites, and reduced the electron transfer resistance, resulting in a superior electrocatalytic activity. Among all the prepared anodes, the Y/3DG-PbO<sub>2</sub>-15 anode exhibited the best activity for electrochemical oxidation of PFOS. After 120 min of electrolysis, the TOC removal efficiency was 80.89% with Y/3DG-PbO<sub>2</sub>-15 anode, greatly higher than 69.13% with 3DG-PbO<sub>2</sub> anode. In addition, the effect of operating parameters on PFOS removal was analyzed by response surface, and the obtained optimum values of current density, initial PFOS concentration, pH, and Na<sub>2</sub>SO<sub>4</sub> concentration were 50 mA/cm<sup>2</sup>, 12.21 mg/L, 5.39, and 0.01 M, respectively. Under the optimal conditions, the PFOS removal efficiency reached up to 97.16% after 40 min of electrolysis. The results of the present study confirmed that the Y/3DG-PbO<sub>2</sub> was a promising anode for electrocatalytic oxidation of persistent organic pollutants.

**Keywords** Electrochemical oxidation, PbO<sub>2</sub> anode, 3DG, Yttrium, PFOS

## Introduction

Perfluorooctane sulfonate (PFOS) is one of the typical perfluoroalkyl substances (PFASs). Due to the unique characteristics of high hydro- and lipo-phobic, good thermal and chemical stability, and excellent surfactant properties, PFOS has been broadly used in industrial applications and the manufacturing processes of daily consumer goods [1, 2]. However, PFOS is easily accumulated in water bodies due to its water solubility and strong persistence [3]. Previous reports indicate that PFOS has been widely distributed around the world and even detected in drinking water and human fluids (serum, breast milk, and urine) [4–6]. In addition,

\*Correspondence:

Limin Chang  
changlimin2139@163.com

<sup>1</sup>Key Laboratory of Preparation and Applications of Environmental Friendly Materials (Jilin Normal University), Ministry of Education, Changchun 130103, China

<sup>2</sup>Key Laboratory of Environmental Materials and Pollution Control, Education Department of Jilin Province, Jilin Normal University, Siping 136000, China

<sup>3</sup>College of Engineering, Jilin Normal University, Siping, Jilin, China



© The Author(s) 2023. **Open Access** This article is licensed under a Creative Commons Attribution 4.0 International License, which permits use, sharing, adaptation, distribution and reproduction in any medium or format, as long as you give appropriate credit to the original author(s) and the source, provide a link to the Creative Commons licence, and indicate if changes were made. The images or other third party material in this article are included in the article's Creative Commons licence, unless indicated otherwise in a credit line to the material. If material is not included in the article's Creative Commons licence and your intended use is not permitted by statutory regulation or exceeds the permitted use, you will need to obtain permission directly from the copyright holder. To view a copy of this licence, visit <http://creativecommons.org/licenses/by/4.0/>. The Creative Commons Public Domain Dedication waiver (<http://creativecommons.org/publicdomain/zero/1.0/>) applies to the data made available in this article, unless otherwise stated in a credit line to the data.

PFOS is one of the environmental endocrine-disrupting chemicals (EDCs) that might induce obesity, cardiovascular problems, cancer, and infertility [7–9]. Therefore, PFOS has posed a great potential threat to the ecological environment and human health, and it is meaningful to explore effective methods to degrade PFOS.

Because of the high energy of C-F bonds (485 kJ/mol) [10], the PFOS has high stability and is extremely resistant to biological degradation. Thus, various methods have been explored to treat PFOS, including physical adsorption [11], constructed wetlands (CWs) [12, 13], photochemical method [14, 15], electrochemical oxidation [16], sonochemical oxidation [17], hydrothermal reaction [18], beams of electron and plasma [19, 20], etc. Among these processes, the electrochemical oxidation process has attracted growing attention due to its excellent oxidation efficiency, mild reaction conditions, simple operation, and environmental compatibility [21, 22]. Shi et al. constructed a reactive electrochemical membrane system, in which  $98.30 \pm 0.51\%$  of PFOS was removed through cross-flow filtration and following electrochemical oxidation processes [23]. Li et al. combined electrochemical oxidation and UV irradiation to treat PFOS, in which the PFOS removal efficiency was significantly greater than the mathematical addition of the solo electrochemical oxidation and UV irradiation systems [24]. The process of adsorption onto graphite intercalated compounds (GIC) and following electrochemical oxidation was proposed by Trzcinski and Harada, and 99% of PFOS was removed with a half-life of 15 min [25]. Yang et al. fabricated a novel Ti/Sn-Sb/SnO<sub>2</sub>-F-Sb anode for electrochemical oxidation of PFOS, and more than 99% of PFOS was removed after 120 min electrolysis [16]. These reports confirm that the electrochemical oxidation process can effectively degrade PFOS either alone or in combination with other technologies.

It is well known that the anode is the heart of electrochemical oxidation, which directly affects the degradation effect of organic pollutants [26, 27]. PbO<sub>2</sub> has been regarded as one of the most popular anode materials because of its easy preparation, low cost, excellent electrocatalytic activity, and high stability [28, 29]. To meet the demand for high electrocatalytic performance for degrading PFOS, we developed a novel three-dimensional graphene-modified lead dioxide (3DG-PbO<sub>2</sub>) anode in our previous study [30]. 3DG significantly increased the electrocatalytic activity of the PbO<sub>2</sub> electrode, which effectively removed PFOS with a degradation rate of 96.17% after 120 min of degradation, much higher than that of pure PbO<sub>2</sub> anode (75.13%) [30]. Nevertheless, we found that the mineralization rate of PFOS was slow for the electrochemical oxidation of PFOS at the 3DG-PbO<sub>2</sub> anode, only 68.58% of TOC was removed after 120 min of electrolysis. Therefore, the better electrocatalytic activity

of 3DG-PbO<sub>2</sub> is needed for the electrochemical oxidation of PFOS.

Rare earth elements have shown superior electrical, thermoelectric, magnetic, optical, and biological properties due to their incompletely occupied 4f electronic configuration, which have been widely used in many fields consisting of electronics, metallurgy, aerospace, photolysis, fuel cell, etc. [31–33]. Some rare earth elements have also been used to improve the activity and stability of PbO<sub>2</sub> anodes. Jin et al. reported that doping Ce and polyvinylpyrrolidone (PVP) into the active layer of  $\beta$ -PbO<sub>2</sub> significantly reduced the charge transfer resistance of the PbO<sub>2</sub> electrode and enhanced the electrocatalytic oxidation performance of the PbO<sub>2</sub> electrode for treating methyl orange dye wastewater [34]. Zhang and co-workers found that doping terbium not only improved the electrocatalytic activity of Ti/PbO<sub>2</sub> anode, but also prolonged its service life to 183 h, 14 times longer than that of Ti/PbO<sub>2</sub> (13 h) [35]. Lan et al. fabricated a Yb-GO-PbO<sub>2</sub> anode, which presented better activity than the pure PbO<sub>2</sub> anode for the degradation of lamivudine [36]. Wang et al. reported that the electrochemical activity of different rare earth elements (La, Ce, Gd, and Er) doped PbO<sub>2</sub> anodes for degradation of *p*-nitrophenol followed the order of Er-PbO<sub>2</sub> > Gd-PbO<sub>2</sub> > La-PbO<sub>2</sub> > Ce-PbO<sub>2</sub> > PbO<sub>2</sub> [37]. Eu-doped PbO<sub>2</sub> anode was also reported to have higher oxygen evolution overpotential, stability, and electrocatalytic activity than the pure PbO<sub>2</sub> anode [38].

As one of the early rare earth metals, Yttrium (Y) has been more and more widely used to promote the activity of various catalysts. Reddy et al. prepared Cu and Y codoped hematite ( $\alpha$ -Fe<sub>2</sub>O<sub>3</sub>) nanostructured photoanodes, and the addition of Y not only increased the electron-hole density of the photoanode but also improved its catalytic activity [39]. Hou et al. synthesized a Y-doped titanium dioxide (nY/TiO<sub>x</sub>) catalyst, which showed superior catalytic activity and higher stability than the pristine TiO<sub>2</sub> catalyst for propane dehydrogenation [40]. The Y<sup>3+</sup> and Co<sup>2+</sup> codoped LaNiO<sub>3</sub> exhibited better activity than pure LaNiO<sub>3</sub> in the photocatalytic degradation of Rhodamine B [41]. The electronic structure of ZnO was changed by doping Y, thereby enhancing the photoelectrochemical performance and prolonging the carrier lifetime of ZnO for water splitting [42]. Yu and coworkers reported that the incorporation of Y<sub>2</sub>O<sub>3</sub> promoted the electrocatalytic activity of the PbO<sub>2</sub> anode due to enhanced electron transfer rate and accelerated generation of reactive oxygen species [43]. Khalfaouy et al. synthesized yttrium-substituted LiMn<sub>1-x</sub>Y<sub>x</sub>PO<sub>4</sub>/C cathode material for lithium-ion batteries, in which yttrium-substituting reduced the charge transfer impedance, improved the lithium-ion diffusion, and the specific discharge capacity of LiMnYPO<sub>4</sub>/C was improved by 14%

[44]. Yttrium-doped  $\text{SnO}_2\text{-NiO}$  nano-composite also exhibited higher specific capacitance and better reversible performance for energy storage applications [45].

Based on the above studies, we predict that Y should be a promising dopant for modifying the  $\text{PbO}_2$  anode, which can productively promote the electrocatalytic activity of the  $\text{PbO}_2$  anode owing to its unique physical and chemical properties. Besides, the ionic radius of  $\text{Y}^{3+}$  ions is much smaller than that of  $\text{Pb}^{2+}$  ions, and close to that of  $\text{Pb}^{4+}$  ions. Consequently, it can easily replace the  $\text{Pb}^{2+}$  into  $\text{PbO}_2$  film and its incorporation will increase the stability of the  $\text{PbO}_2$  film [46, 47]. Herein, in this work, the rare earth metal element of Y was selected as a dopant to be codoped into the  $\text{PbO}_2$  anode with 3DG (the anode was denoted by  $\text{Y/3DG-PbO}_2$ ) by the composite electrodeposition method. The effect of doping Y on the surface micromorphology, crystal structure, and elemental chemical state of the 3DG- $\text{PbO}_2$  anode was analyzed by scanning electron microscopy (SEM), X-ray diffraction (XRD), and X-ray photoelectron spectroscopy (XPS). The electrochemical performance of the  $\text{Y/3DG-PbO}_2$  anode was investigated by linear sweep voltammetry (LSV), cyclic voltammetry (CV), electrochemical impedance spectroscopy (EIS), and Tafel. In addition, the electrocatalytic oxidation behavior of perfluorooctane sulfonate (PFOS) at  $\text{Y/3DG-PbO}_2$  anode was investigated intensively.

## Experimental

### Materials

Pure titanium sheets were obtained from Jinkai Co., Ltd. (Baoji, China).  $\text{Y}(\text{NO}_3)_3 \cdot 6\text{H}_2\text{O}$ , L-ascorbic acid, and PFOS were purchased from Energy Chemical (Shanghai, China).  $\text{Pb}(\text{NO}_3)_2$ ,  $\text{SnCl}_4 \cdot 5\text{H}_2\text{O}$ ,  $\text{SbCl}_3$ ,  $\text{Na}_2\text{SO}_4$ ,  $\text{C}_3\text{H}_7\text{OH}$ ,  $\text{HNO}_3$ ,  $\text{H}_2\text{C}_2\text{O}_4$ , and  $\text{HCl}$  were provided by Sinopharm (Shanghai, China).  $\text{NaF}$  and  $\text{PbO}$  were supplied by Shenyang Chemical Reagent Factory (Shenyang, China). All chemicals used were analytical reagents and used directly without any further purification. All the solutions were prepared with deionized water.

### Preparation of $\text{Y/3DG-PbO}_2$ anode

The preparation process of  $\text{Y/3DG-PbO}_2$  anodes was followed as that of 3DG- $\text{PbO}_2\text{-0.08}$  anode in our previous study [30], consisting of pretreatment, thermal deposition of  $\text{SnO}_2\text{-Sb}_2\text{O}_3$  bottom layer, electrodeposition of  $\alpha\text{-PbO}_2$  intermediate layer and electrodeposition of  $\beta\text{-PbO}_2$  active layer. Different from the preparation process of 3DG- $\text{PbO}_2\text{-0.08}$ , the electroplating solution of the active layers of  $\text{Y/3DG-PbO}_2$  anodes contained 5, 15, or 30  $\mu\text{M}$   $\text{Y}(\text{NO}_3)_3$ . The obtained anodes were named  $\text{Y/3DG-PbO}_2\text{-5}$ ,  $\text{Y/3DG-PbO}_2\text{-15}$ , and  $\text{Y/3DG-PbO}_2\text{-30}$ , respectively. For morphological comparison, the pure  $\text{PbO}_2$ ,  $\text{Y-PbO}_2\text{-5}$ ,  $\text{Y-PbO}_2\text{-15}$ , and  $\text{Y-PbO}_2\text{-30}$  anodes were

also fabricated, whose preparation process was the same as those of 3DG- $\text{PbO}_2$ ,  $\text{Y/3DG-PbO}_2\text{-5}$ ,  $\text{Y/3DG-PbO}_2\text{-15}$ , and  $\text{Y/3DG-PbO}_2\text{-30}$  anodes, respectively except that no 3DG was added to the electroplating solution of the active layer.

### Analytical methods

A scanning electron microscope (JEOL JSM-6510) was used to characterize the surface morphology of anodes. X-ray diffractometer (PC 2500, Rigaku) equipped with  $\text{Cu K}\alpha$  irradiation ( $\lambda=0.154060$  nm) was used to analyze the phase composition of samples with a scanning rate of  $16^\circ/\text{min}$ . XPS was carried on an ESCALAB250XI X-ray photoelectron spectrometer equipped with  $\text{Al K}\alpha$  radiation (1486.60 eV, 150 W) to analyze the chemical state of elements on the surface of electrodes.

All the electrochemical tests including LSV, CV, EIS, and Tafel were performed on an electrochemical workstation (IVIUMSTAT, Netherlands) in 0.5 M  $\text{H}_2\text{SO}_4$  solution with a standard three-electrode system. The as-prepared anodes were used as the working electrodes, a platinum sheet as the auxiliary electrode, and a saturated calomel electrode as the reference electrode. The LSV was tested in the potential range from 1 to 2.5 V with a scan rate of 50 mV/s. The CV was tested at scan rates of 20, 40, 60, 80, and 100 mV/s in a potential range of 0.5–2.0 V. The EIS was tested in a frequency range from 0.01 to  $10^4$  Hz with an applied sine wave of 10 mV amplitude. The Tafel curves were obtained in a potential range from 1.0 to 1.6 V and at a scan rate of 0.166 mV/s.

The active species were measured on a Hitachi JES-FA200 electron spin resonance (ESR) spectrometer. Since the terephthalic acid (TA) can easily react with  $\bullet\text{OH}$  radicals to form the fluorescent 2-hydroxyterephthalic acid (2-HA), it was used as a probe molecule to test the  $\bullet\text{OH}$  radical generation of prepared anodes. The concentration of 2-HA was measured on a fluorescence spectrophotometer (Cary EclipseG9800A, Agilent,  $\lambda_{\text{ex}}=315$  nm and  $\lambda_{\text{em}}=425$  nm). The  $\bullet\text{OH}$  radical generation experiments were conducted at a constant current density of  $30 \text{ mA/cm}^2$  in 100 mL of 0.75 mM TA+0.25 M  $\text{Na}_2\text{SO}_4$  + 0.5 g/L NaOH solution at a temperature of 30 °C. 0.8 mL of electrolyte was drawn at five-minute intervals and diluted 5 times with deionized water.

The concentrations of PFOS were analyzed on a liquid chromatography-mass spectrometry (LC-MS/MS, Agilent 6120) with an XBridge C18 column (4.6 mm $\times$ 150 mm, 3.5  $\mu\text{L}$ ). Gradient mobile elution was delivered at a flow rate of 1.5 mL/min which was composed of eluent A (10 mM ammonium acid carbonate in 100% water) and eluent B (100% acetonitrile). In the initial 2.0 min, the acetonitrile gradient was increased from 5% to 95%. In 2.0–12.0 min, the acetonitrile was held at

95% for 10 min. The PFOS removal efficiency was calculated according to Eq. (1):

$$r = \frac{C_0 - C_t}{C_0} \times 100\% \quad (1)$$

where  $r$  is the removal efficiency of PFOS,  $C_0$  is the initial PFOS concentration, and  $C_t$  is the PFOS concentration at a given time  $t$ . The TOC value of the degradation solution was measured on a TOC analyzer (Vario TOC). The TOC removal efficiency was calculated according to Eq. (2).

$$\eta = \frac{\text{TOC}_0 - \text{TOC}_t}{\text{TOC}_0} \times 100\% \quad (2)$$

where  $\eta$  is the TOC removal efficiency,  $\text{TOC}_0$  is the initial TOC concentration of PFOS solution, and  $\text{TOC}_t$  is the TOC concentration at a given time  $t$ . The energy consumption (EC) on each anode was calculated to evaluate the energy efficiency of PFOS degradation according to Eq. (3) [48].

$$EC = \frac{(U_{\text{cell}}I) t_{90\%}}{V} \quad (3)$$

where  $U_{\text{cell}}$  is the average cell voltage (V),  $I$  is the applied current (A),  $t_{90\%}$  is the time for 90% PFOS removal (h), and  $V$  is the volume of PFOS solution ( $\text{m}^3$ ). The concentration of  $\text{Pb}^{2+}$  ions in the degradation solution was determined on an Agilent 7500 inductively coupled plasma mass spectrometer (ICP-MS).

### Electrochemical oxidation of PFOS

The electrocatalytic oxidation of PFOS was performed in 200 mL of organic glass reactor with continuous

magnetic stirring at a constant temperature of 30 °C. The initial PFOS concentration was 50 mg/L, 0.05 M  $\text{Na}_2\text{SO}_4$  was used as the supporting electrolyte, and the applied current density was 30  $\text{mA}/\text{cm}^2$ . The as-prepared Y/3DG-PbO<sub>2</sub> or 3DG-PbO<sub>2</sub> electrode with an effective area of 3 cm × 5 cm served as the anode. The ratio of electrode surface area to working volume was 3/40  $\text{cm}^2/\text{mL}$ . Since only hydrogen evolution reaction occurs on the cathode, which doesn't participate in the degradation process [49], a conductive stainless steel sheet with the same area as the anode was used as the cathode. Two electrodes were positioned vertically and parallel to each other with an inter-distance of 2 cm.

## Results and discussion

### Characterization of Y/3DG-PbO<sub>2</sub> electrode

SEM analysis was carried out to observe the surface morphology of the prepared Y/3DG-PbO<sub>2</sub> anodes. For comparison, the SEM images of pure PbO<sub>2</sub> and Y-PbO<sub>2</sub> anodes were also presented in Fig. 1a-d. It can be observed that the surface of pure PbO<sub>2</sub> electrode was composed of unevenly sized pyramidal crystals (Fig. 1a). After adding 5 or 15  $\mu\text{M}$   $\text{Y}^{3+}$ , the crystal size of the  $\beta$ -PbO<sub>2</sub> gradually decreased and the crystals were more compact (Fig. 1b and c). However, when the concentration of  $\text{Y}^{3+}$  was further improved to 30  $\mu\text{M}$ , the crystal size of the  $\beta$ -PbO<sub>2</sub> became uneven, and some crystals stacked together (Fig. 1d). Compared to the pure PbO<sub>2</sub> and Y-PbO<sub>2</sub> anodes, the morphology of 3DG-PbO<sub>2</sub> and Y/3DG-PbO<sub>2</sub> was evident, where PbO<sub>2</sub> particles were well wrapped by graphene sheets (Fig. 1e-h). This indicated that a strong coupling was formed between the graphene sheets and PbO<sub>2</sub> particles. It also can be seen that the crystal sizes of Y/3DG-PbO<sub>2</sub> anodes were greatly smaller than those of pure PbO<sub>2</sub> and Y-PbO<sub>2</sub> anodes, which may be due to that the graphene sheets acted as

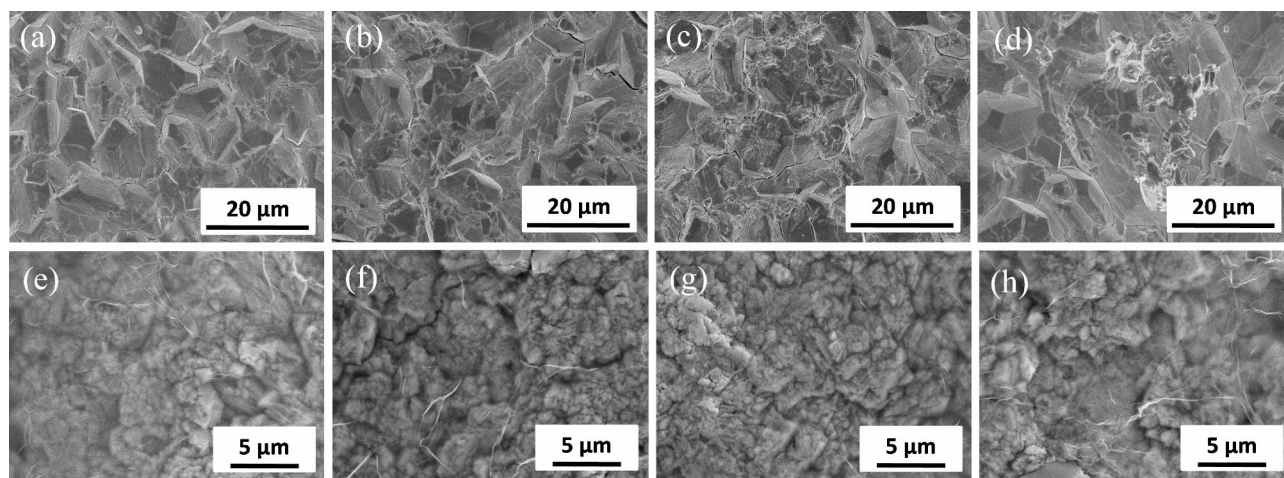


**Fig. 1** SEM images of pure PbO<sub>2</sub> (a), Y-PbO<sub>2</sub>-5 (b), Y-PbO<sub>2</sub>-15 (c), Y-PbO<sub>2</sub>-30 (d), 3DG-PbO<sub>2</sub> (e), Y/3DG-PbO<sub>2</sub>-5 (f), Y/3DG-PbO<sub>2</sub>-15 (g), and Y/3DG-PbO<sub>2</sub>-30 (h) electrodes

support template for growing the  $\text{PbO}_2$  crystals [50]. Among three Y/3DG- $\text{PbO}_2$  anodes, the Y/3DG- $\text{PbO}_2$ -15 anode possessed the most uniform, flat, and dense surface, which was consistent with the better surface of the Y- $\text{PbO}_2$ -15 anode.

The effect of doped Y on the crystal phase structure of the 3DG- $\text{PbO}_2$  anode was investigated by XRD. Figure 2(a) shows the XRD patterns of 3DG- $\text{PbO}_2$ , Y/3DG- $\text{PbO}_2$ -5, Y/3DG- $\text{PbO}_2$ -15, and Y/3DG- $\text{PbO}_2$ -30 anodes. All the anodes presented characteristic diffraction peaks at  $2\theta=25.3^\circ$ ,  $31.9^\circ$ ,  $36.1^\circ$ ,  $49.1^\circ$ ,  $58.8^\circ$ ,  $62.5^\circ$ , and  $85.6^\circ$ , which are well indexed to the (110), (101), (200), (211), (310), (301), and (411) planes of  $\beta$ - $\text{PbO}_2$  crystals (JCPDS card no. 76-0564) [27, 51, 52]. This demonstrates that doping Y didn't affect the formation of  $\beta$ - $\text{PbO}_2$  crystals. It also can be observed from Fig. 2(a) that the diffraction peak intensity of the (200) plane of 3DG- $\text{PbO}_2$  was significantly increased after doping Y, while the diffraction peak intensities of (110), (101), (211), and (301) planes were reduced. This phenomenon indicates that doping Y changed the preferred growth orientation of  $\beta$ - $\text{PbO}_2$ , which may influence the electro-catalytic activity of the 3DG- $\text{PbO}_2$  anode [27].

XPS measurements were performed to investigate the chemical states of elements on the surface of 3DG- $\text{PbO}_2$  and Y/3DG- $\text{PbO}_2$ -15 anodes. As shown in Fig. 2(b), both of the high-resolution XPS spectra of 3DG- $\text{PbO}_2$  and Y/3DG- $\text{PbO}_2$ -15 anodes consisted of splitting peaks of Pb  $4f_{7/2}$  and Pb  $4f_{5/2}$ , which were fitted into four peaks at about 137.0, 137.9, 141.9 and 142.8 eV, indicating

presence of  $\text{Pb}^{4+}$  and  $\text{Pb}^{2+}$  ions in  $\text{PbO}_2$  films [53, 54]. The peaks at 137.1 eV and 141.9 eV are attributed to Pb (IV), in agreement with the spectral values for  $\text{PbO}_2$  [55, 56], while the peaks at 137.9 eV and 142.8 eV are assigned to the binding energy of Pb (II). This demonstrates the presence of PbO or  $\text{Pb}_3\text{O}_4$  ( $2\text{PbO}\cdot\text{PbO}_2$ ) compounds in the 3DG- $\text{PbO}_2$  and Y/3DG- $\text{PbO}_2$ -15 films [57]. Y 3d spectrum of the Y/3DG- $\text{PbO}_2$ -15 anode is displayed in Fig. 2(c). Two main components attributed to Y  $3d_{5/2}$  and Y  $3d_{3/2}$  can be observed at the binding energies of 156.9 and 159.2 eV, respectively, meaning that Y was doped into the  $\beta$ - $\text{PbO}_2$  film in the state of  $\text{Y}_2\text{O}_3$  [53, 58]. As shown in Fig. 2(d and e), the high-resolution O 1s XPS spectra of 3DG- $\text{PbO}_2$  and Y/3DG- $\text{PbO}_2$ -15 anodes were fitted into three characteristic peaks, in which the peaks at 529.0 eV (Fig. 2(d)) and 529.1 eV (Fig. 2(e)) are ascribed to the lattice oxygen ( $\text{O}_L$ ) [59], the peaks of 530.9 eV (Fig. 2(d)) and 530.6 eV (Fig. 2(e)) are indexed to the adsorbed hydroxyl oxygen ( $\text{O}_{\text{OH}}$ ) species [42, 60], and the peaks of 532.6 eV (Fig. 2(d)) and 531.8 eV (Fig. 2(e)) are attributed to the adsorbed  $\text{H}_2\text{O}$  ( $\text{O}_{\text{H}_2\text{O}}$ ) [61]. In the electrocatalytic oxidation process, the hydroxyl groups can be transformed to  $\bullet\text{OH}$  radicals. In general, a high proportion of  $\text{O}_{\text{OH}}$  species favors the production of more  $\bullet\text{OH}$  radicals. Thus, the proportions of different oxygen species were calculated according to their peak areas. As a result, the proportions of  $\text{O}_L$ ,  $\text{O}_{\text{OH}}$ , and  $\text{O}_{\text{H}_2\text{O}}$  in the Y/3DG- $\text{PbO}_2$ -15 film were 44.19%, 35.86%, and 28.85%, while those in the 3DG- $\text{PbO}_2$  film were 31.86%, 36.39%, and 31.75%.

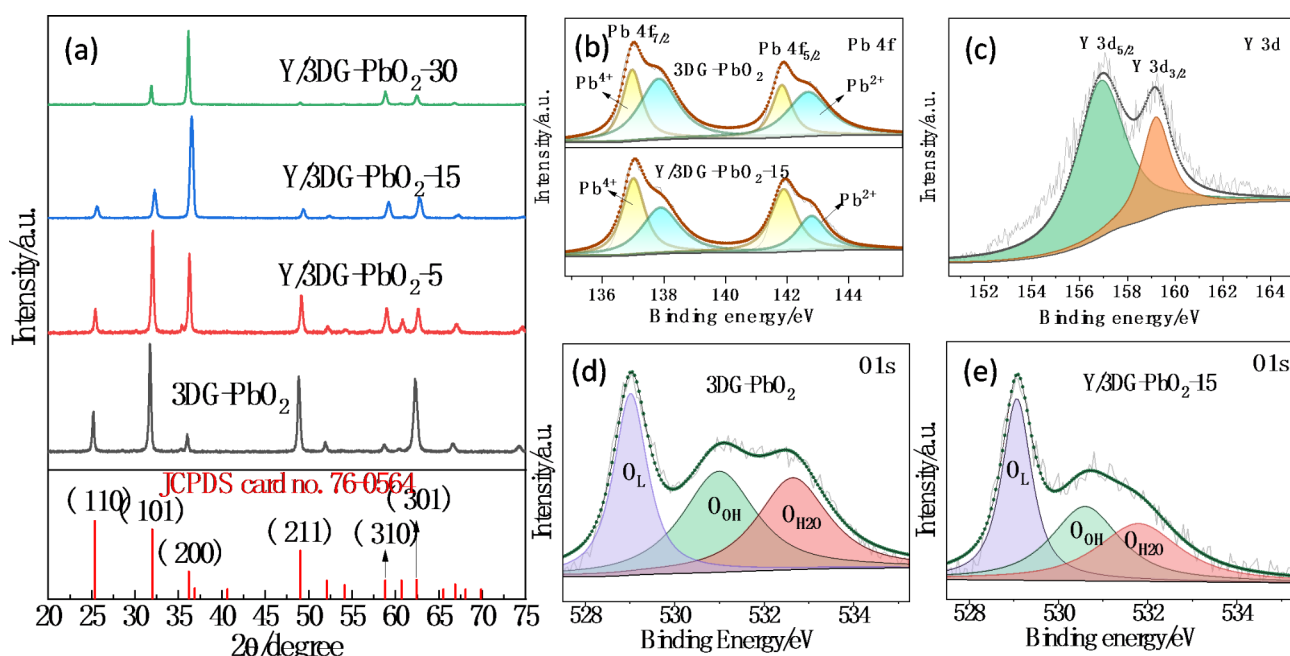


**Fig. 2** (a) XRD patterns of prepared anodes, XPS spectra of Pb 4f for 3DG- $\text{PbO}_2$  and Y/3DG- $\text{PbO}_2$ -15 anodes (b), Y 3d for Y/3DG- $\text{PbO}_2$ -15 anode (c), and O 1s for 3DG- $\text{PbO}_2$  (d) and Y/3DG- $\text{PbO}_2$ -15 (e) anodes

respectively. This result indicates that doping Y cannot improve the content of  $O_{OH}$  in the 3DG-PbO<sub>2</sub> film.

### Electrochemical characterization

In the process of electrochemical oxidation, hydroxyl ( $\cdot OH$ ) radicals are continuously generated on the surface of the anode, which plays the most key role in the degradation of pollutants. The oxygen evolution potential (OEP) is one of the important electrochemical indicators to evaluate the ability of hydroxyl radical generation. In general, high oxygen evolution potential (OEP) can inhibit the occurrence of oxygen evolution reaction, being beneficial to the accumulation of more  $\cdot OH$  radicals [54, 62, 63]. Thus, the OEP values of the as-prepared anodes were measured by LSV. As shown in Fig. 3(a), the OEP of the Y/3DG-PbO<sub>2</sub>-15 anode is 2.04 V, higher than those of 3DG-PbO<sub>2</sub> (1.96 V), Y/3DG-PbO<sub>2</sub>-5 (1.98 V) and Y/3DG-PbO<sub>2</sub>-30 (1.99 V) anodes. Therefore, the OEP of the 3DG-PbO<sub>2</sub> anode was increased by doping

Y<sup>3+</sup>. The electrochemical activity of the anode is associated with the surface active sites of an electrode, which can be assessed by the voltammetric charge ( $q^*$ ) [37]. In general, anodes with higher  $q^*$  have higher electrocatalytic activity [64]. Thus, CV tests were conducted in 0.5 M H<sub>2</sub>SO<sub>4</sub> solution at scan rates of 20, 40, 60, 80, and 100 mV/s to assess the electrochemical activity of the prepared anodes. The obtained CV voltammograms are shown in Fig. S1 of supporting materials (SM). It can be observed that all the CV curves yielded a couple of redox peaks, which are ascribed to the reversible Pb<sup>2+</sup>/Pb<sup>4+</sup> reaction [56, 65]. The  $q^*$  values of all the CV curves were calculated using Eq. (4).

$$q^* = \frac{\int idV}{v} \quad (4)$$

where  $\int IDV$  is the integrated area of the CV curve and  $v$  is the scan rate. As displayed in Fig. 3(b), the  $q^*$  values

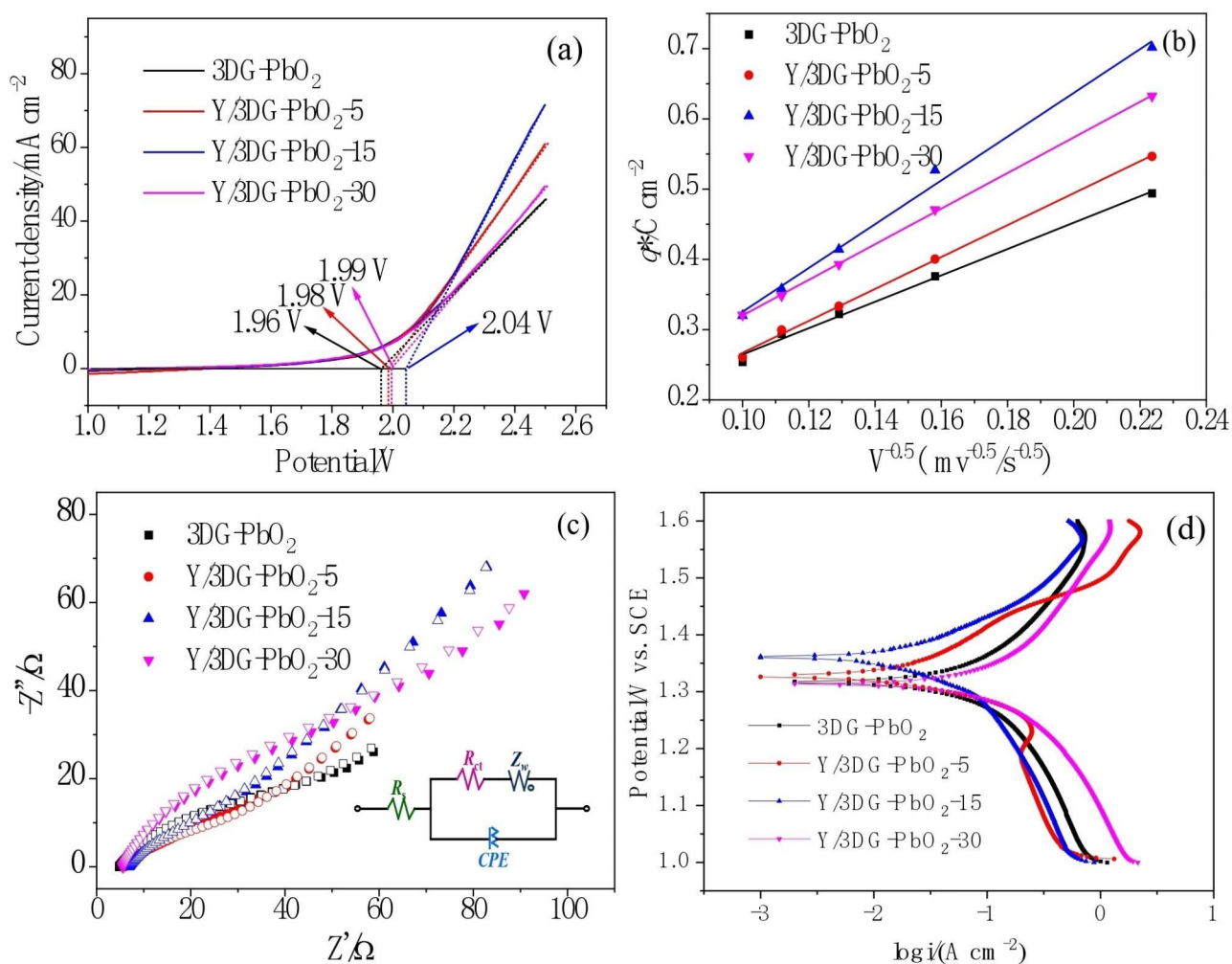


**Fig. 3** LSV curves (a),  $q^*$  against for  $v^{-1/2}$  (b), Nyquist diagrams (c), and Tafel curves (d) of 3DG-PbO<sub>2</sub> and Y/3DG-PbO<sub>2</sub> electrodes measured in 0.5 mol/L H<sub>2</sub>SO<sub>4</sub> solution

of four anodes followed the order of  $Y/3DG-PbO_2-15 > Y/3DG-PbO_2-30 > Y/3DG-PbO_2-5 > 3DG-PbO_2$ , suggesting that doping Y promoted the number of active sites of the  $3DG-PbO_2$  anode and the  $Y/3DG-PbO_2-15$  electrode possessed more active sites than other three anodes. The influence of Y on the charge transfer resistance of the  $3DG-PbO_2$  electrode was analyzed by EIS in  $0.5\text{ M H}_2\text{SO}_4$  at open circuit potential. Figure 3(c) shows the Nyquist diagrams of  $3DG-PbO_2$ ,  $Y/3DG-PbO_2-5$ ,  $Y/3DG-PbO_2-15$ , and  $Y/3DG-PbO_2-30$  electrodes. To obtain the charge transfer resistance of four electrodes, the Nyquist diagrams were fitted by the equivalent circuit model (the inset of Fig. 3(c)), where  $R_s$ ,  $R_{CT}$ ,  $Z_w$ , and  $CPE$  represent the solution resistance, charge transfer resistance at the solution/electrode surface, Warburg impedance, and the constant phase element, respectively. The  $R_{ct}$  values of  $Y/3DG-PbO_2-5$  and  $Y/3DG-PbO_2-15$  electrodes were  $33.54$  and  $27.22\ \Omega/\text{cm}^2$ , respectively, lower than that of the  $3DG-PbO_2$  electrode ( $45.31\ \Omega/\text{cm}^2$ ), indicating that doping Y reduced the charge transfer resistance during the electrochemical reaction process. However, the  $R_{ct}$  value of the  $Y/3DG-PbO_2-30$  electrode was  $61.13\ \Omega/\text{cm}^2$ , higher than that of the  $3DG-PbO_2$  electrode. This may be related to the uneven surface of the  $Y/3DG-PbO_2-30$  electrode.

To investigate the influence of doping Y on the stability of the  $3DG-PbO_2$  anode, a potentiodynamic polarization test was carried out in  $0.5\text{ M H}_2\text{SO}_4$  solution with the scan potential range from  $1.0$  to  $1.6\text{ V}$  vs. SCE at a scan rate of  $0.166\text{ mV/s}$ . The obtained Tafel curves are shown in Fig. 3d. The self-corrosion potential and self-corrosion current density were obtained by fitting the curves in the strong polarization region, which were ( $1.317\text{ V}$ ,  $68.76\ \mu\text{A}/\text{cm}^2$ ), ( $1.326\text{ V}$ ,  $22.70\ \mu\text{A}/\text{cm}^2$ ), ( $1.360\text{ V}$ ,  $47.15\ \mu\text{A}/\text{cm}^2$ ), and ( $1.315\text{ V}$ ,  $11.78\ \mu\text{A}/\text{cm}^2$ ) for  $3DG-PbO_2$ ,  $Y/3DG-PbO_2-5$ ,  $Y/3DG-PbO_2-15$ , and  $Y/3DG-PbO_2-30$ , respectively. Compared to the  $3DG-PbO_2$  electrode, the  $Y/3DG-PbO_2-5$  and  $Y/3DG-PbO_2-15$  electrodes possessed higher self-corrosion potential and lower self-corrosion current density, indicating that doping Y promoted the stability of the  $3DG-PbO_2$  electrode [60, 66]. The higher stability of  $Y/3DG-PbO_2-5$  and  $Y/3DG-PbO_2-15$  was attributed to their more compact surface, which effectively prevented the electrolyte from entering the inside of the  $PbO_2$  film [67]. However, it also can be found that the  $Y/3DG-PbO_2-30$  electrode had lower self-corrosion potential and higher self-corrosion current density than the  $3DG-PbO_2$  electrode, meaning that doping excessive Y would cause the decrease in compactness of the  $PbO_2$  film and the reduction the stability of  $3DG-PbO_2$  electrode.

### Generation of reactive oxidants

The reactive oxidants are responsible for the degradation of organic pollutants in the electrochemical oxidation process [68, 69]. The ESR technique was applied to reveal the possible reactive oxidant species formed in the electrochemical system with  $Y/3DG-PbO_2-15$  anode, in which the DMPO was used as spin-trapping reagent of  $\bullet\text{OH}$ ,  $\bullet\text{SO}_4^{2-}$  and  $\bullet\text{O}_2^-$  radicals. As shown in Fig. 4(a), no distinctive DMPO- $\bullet\text{O}_2^-$  signal was observed in this electrochemical system. Instead, the strong characteristic patterns of DMPO- $\bullet\text{OH}$  with quartet signals of an intensity ratio of  $1:2:2:1$  were observed, confirming the generation of  $\bullet\text{OH}$  radicals [70]. The DMPO- $\bullet\text{SO}_4^{2-}$  signals were also observed in Fig. 4(a), but their intensity was lower than those of DMPO- $\bullet\text{OH}$ , meaning production of less  $\bullet\text{SO}_4^{2-}$  radicals. Therefore, the  $\bullet\text{OH}$  radical is the predominant reactive oxidizing species in this electrochemical oxidation process. To analyze the influence of doping Y on the  $\bullet\text{OH}$  radical generation performance of the  $3DG-PbO_2$  anode, the TA was used as a quenching agent to measure the  $\bullet\text{OH}$  radical generation amount in the  $3DG-PbO_2$  and  $Y/3DG-PbO_2-15$  systems, in which the TA can quickly react with  $\bullet\text{OH}$  radicals to form a fluorescent product of 2-HA [71]. As shown in Fig. 4(b and c), the fluorescent peak appeared at around  $425\text{ nm}$  and its intensity gradually increased with extending electrolysis time for both  $3DG-PbO_2$  and  $Y/3DG-PbO_2-15$  anodes, demonstrating that the  $\bullet\text{OH}$  radicals generated continuously on the surface of these two anodes. Figure 4(d) provides the linear relations between the concentration of  $\bullet\text{OH}$  radicals and electrolysis time. The higher rate constant of  $\bullet\text{OH}$  radical generation ( $k_{\text{OH}}$ ) of  $0.155\ \mu\text{M}/\text{min}$  was achieved by the  $Y/3DG-PbO_2-15$  anode than that of the  $3DG-PbO_2$  anode ( $0.144\ \mu\text{M}/\text{min}$ ), demonstrating that doping Y promoted the  $\bullet\text{OH}$  radical generation ability of  $3DG-PbO_2$  anode, and the  $Y/3DG-PbO_2-15$  should have higher electrocatalytic activity for degrading PFOS. Combined with the above XPS result that the Y didn't improve the content of  $\text{O}_{\text{OH}}$  in the  $3DG-PbO_2$  film, it can be concluded that the improvement of  $\bullet\text{OH}$  radical generation ability of  $3DG-PbO_2$  anode by doping Y was mainly due to the improvement of the OEP from  $1.96$  to  $2.04\text{ V}$ .

### Electrochemical oxidation of PFOS

The electrocatalytic performance of  $3DG-PbO_2$ ,  $Y/3DG-PbO_2-5$ ,  $Y/3DG-PbO_2-15$ , and  $Y/3DG-PbO_2-30$  anodes for degrading PFOS is presented in Fig. 5. Figure 5(a) shows the removal efficiency of PFOS on four anodes with the extension of electrolysis time. It can be observed that the  $Y/3DG-PbO_2-15$  anode exhibited excellent catalytic performance and achieved  $99.57\%$  of PFOS removal efficiency, followed by  $Y/3DG-PbO_2-5$  ( $97.32\%$ ),  $3DG-PbO_2$  ( $96.17\%$ ), and  $Y/3DG-PbO_2-30$  ( $93.51\%$ )

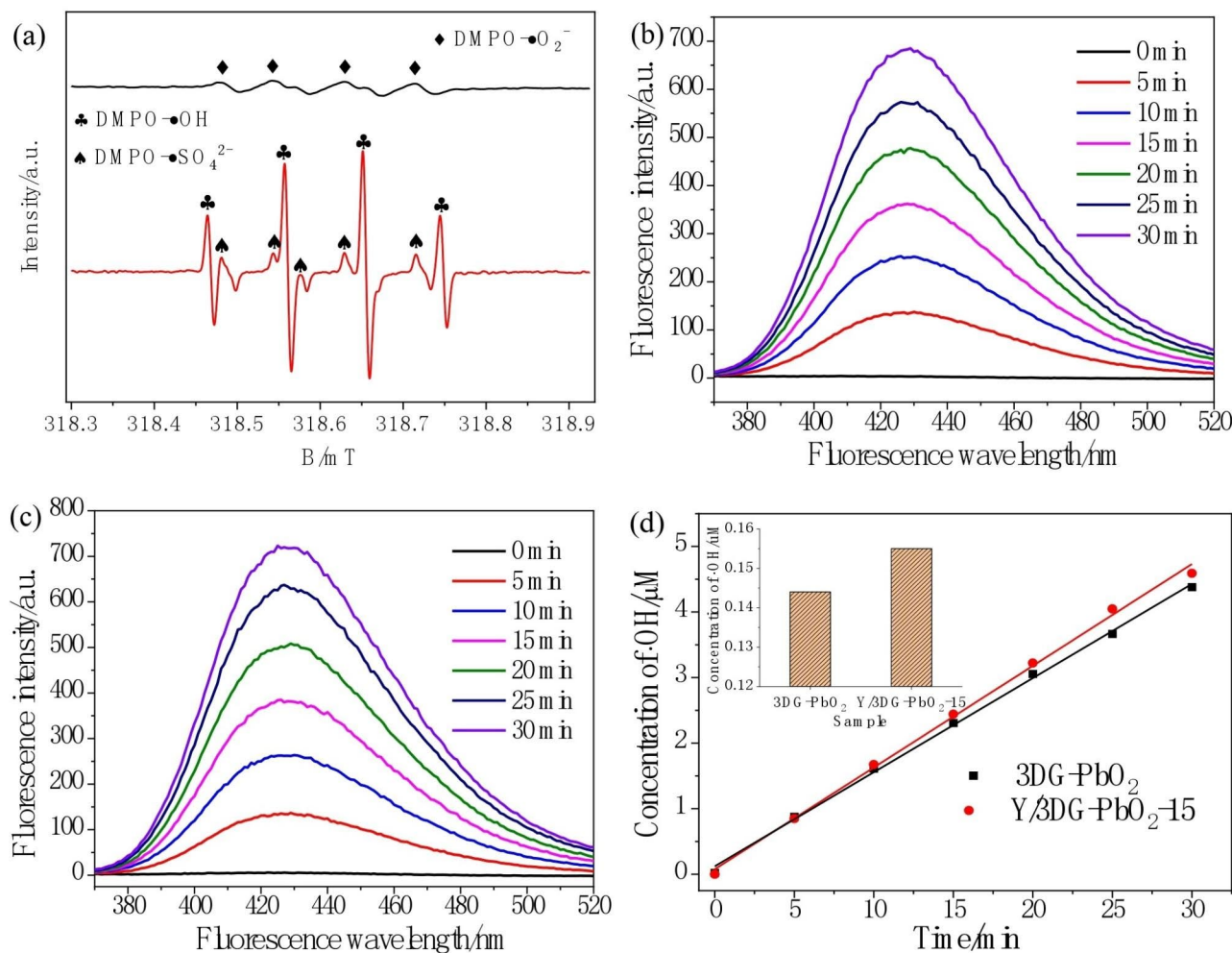


**Fig. 4** ESR spectra of the free radicals trapped by DMPO in electrochemical oxidation process with Y/3DG-PbO<sub>2</sub>-15 anode (a), fluorescent spectra of electrolysis solution of 3DG-PbO<sub>2</sub> (b) and Y/3DG-PbO<sub>2</sub>-15 (c) anodes, and evolution of  $\cdot\text{OH}$  radical concentration with electrolysis time for 3DG-PbO<sub>2</sub> and Y/3DG-PbO<sub>2</sub>-15 anodes (d)

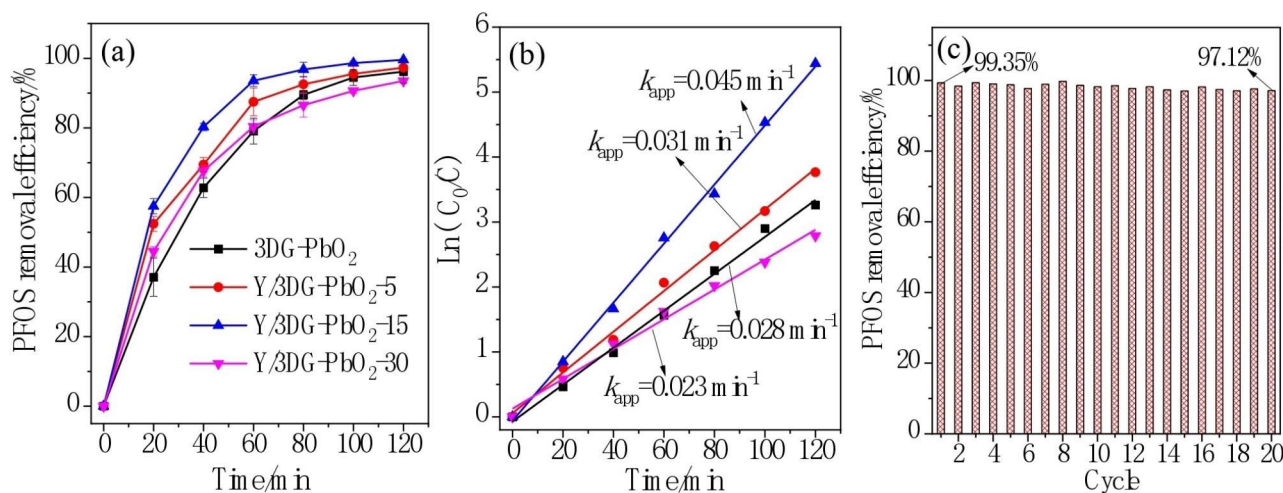


**Fig. 5** Variation curves of PFOS removal efficiency at different anodes (a), kinetic analysis curves (b), and electrochemical degradation of PFOS for twenty successive cycles using Y/3DG-PbO<sub>2</sub>-15 anode (c)

anodes. Figure 5(b) provides the results obtained from the kinetic analysis. The electrocatalytic oxidation process of PFOS can be well described by the pseudo-first-order kinetic equation, and the pseudo first order rate constants ( $k_{app}$ ) of 3DG-PbO<sub>2</sub>, Y/3DG-PbO<sub>2</sub>-5, Y/3DG-PbO<sub>2</sub>-15, and Y/3DG-PbO<sub>2</sub>-30 anodes were 0.028, 0.031, 0.045, and 0.023 min<sup>-1</sup>, respectively. The electrochemical oxidation of PFOS has also been reported in some literature. Zhuo et al. prepared a Ti/TiO<sub>2</sub>-NTs/Ag<sub>2</sub>O/PbO<sub>2</sub> anode for electrochemical degradation of PFOS, and 74.87% of PFOS (90 mL of 0.0929 mM) degradation ratio was obtained after 180 min of electrolysis [72]. Zhuo and coworkers also reported an 89% PFOS removal ratio on a Ti/SnO<sub>2</sub>-Sb<sub>2</sub>O<sub>3</sub>/PbO<sub>2</sub>-PTFE anode after 3 h of electrochemical treatment [73]. 30% and 99% PFOS (20 μM) were removed after 4 and 14 h electrolysis in an electrochemical oxidation process on a Ti<sub>4</sub>O<sub>7</sub> anode, respectively [48]. The high removal efficiency of 99.57% after 120 min of electrolysis obtained by Y/3DG-PbO<sub>2</sub>-15 anode was significantly higher than those reported in the above literature. To compare the energy efficiency of PFOS degradation at the Y/3DG-PbO<sub>2</sub> anodes with that reported in previous study [48], the EC values were calculated by Eq. (3) to be 16.6, 13.9, 10.5, and 19.1 kWh/m<sup>3</sup> for 3DG-PbO<sub>2</sub>, Y/3DG-PbO<sub>2</sub>-5, Y/3DG-PbO<sub>2</sub>-15, and Y/3DG-PbO<sub>2</sub>-30 anodes, respectively with corresponding average cell potential of 5.4, 5.3, 5.1, and 5.2 V. It can be found that the EC (10.5 kWh/m<sup>3</sup>) of Y/3DG-PbO<sub>2</sub>-15 anode was significantly lower than ~20 kWh/m<sup>3</sup> of Micro-Ti<sub>4</sub>O<sub>7</sub> anode at the cell potential of ~5 V [48].

To evaluate the mineralization degree of PFOS with Y/3DG-PbO<sub>2</sub> anodes, the TOC values of PFOS degradation solution were also measured and TOC removal efficiencies were calculated. After 120 min of electrolysis, the TOC removal efficiencies were 69.13%, 73.62%, 80.89%, and 65.41% with 3DG-PbO<sub>2</sub>, Y/3DG-PbO<sub>2</sub>-5, Y/3DG-PbO<sub>2</sub>-15, and Y/3DG-PbO<sub>2</sub>-30 anodes, respectively. Higher TOC removal efficiencies of Y/3DG-PbO<sub>2</sub>-5 and Y/3DG-PbO<sub>2</sub>-15 anodes than those of 3DG-PbO<sub>2</sub> anode demonstrated that doping Y greatly improved the mineralization ability of 3DG-PbO<sub>2</sub> anode.

Above results confirmed that the Y/3DG-PbO<sub>2</sub>-15 anode had more outstanding electrocatalytic activity for degrading PFOS than the other three anodes. This could be explained by its higher OEP, more active sites, smaller charger transfer resistance, and stronger •OH radicals generation ability.

In addition to high catalytic activity, good reusability is one of the important requirements for the practical application of the PbO<sub>2</sub> anode [74]. The reusability of the Y/3DG-PbO<sub>2</sub>-15 anode was evaluated using consecutive electrolysis of PFOS. Figure 5(c) presents the removal percentages of PFOS over the Y/3DG-PbO<sub>2</sub>-15 anode after 120 min of electrolysis in twenty cycles. It can be

observed that the change in PFOS removal efficiency within 20 consecutive cycles of electrolysis was slight. The removal efficiency of PFOS of the 20th cycle was 97.12%, slightly lower than 99.35% of the first cycle, demonstrating excellent reusability of the Y/3DG-PbO<sub>2</sub>-15 anode. To assess the safety of electrochemical degradation of PFOS with Y/3DG-PbO<sub>2</sub>-15 anode, the concentration of Pb<sup>2+</sup> ions in the electrolyte was measured by ICP. After 120 min of electrolysis, the concentration of Pb<sup>2+</sup> ions was 0.004 mg/L, far below the 0.01 mg/L of the Drinking-water Quality of WHO [71], indicating the safety of this process.

The response surface methodology (RSM) was used to describe the interaction between the response value (PFOS removal efficiency) and operating parameters (current density, initial PFOS concentration, pH, and Na<sub>2</sub>SO<sub>4</sub> concentration) assisted with the BOX-Behnken method. The independent variables and designed 29 experimental sets are listed in Table S1 and Table S2 of SM, respectively. To obtain a precise model, parameters with a p-value > 0.05 were excluded from the model [75]. Thus, the quadratic polynomial model for PFOS removal efficiency (%) was presented as Eq. (5).

PFOS removal efficiency (%) = 86.98 + 10.56A - 15.48B - 8.16C + 2.03D - 4.61AD - 7.63A<sup>2</sup> - 5.71B<sup>2</sup> - 3.85C<sup>2</sup> (5).

The ANOVA results are listed in Table S3. A large F-value of 19.63 and p-value < 0.0001 indicated the model was highly meaningful for fitting the actual data [76]. The values of R<sup>2</sup> (0.9515) and adj-R<sup>2</sup> (0.9030) were close to unity and the F-value and p-value for Lack of Fit are 4.00 and 0.0970, respectively, meaning the high correlation between the experimental and the predicted removal efficiency of PFOS [77]. The value of adequate precision (14.999) was larger than 4, indicating the signal-to-noise of the model was adequate. The coefficient of variation (C.V.) was 6.35, less than the critical value of 10%, implying the high reproducibility of the model. The F-values of current density, initial PFOS concentration, pH, and Na<sub>2</sub>SO<sub>4</sub> concentration were 39.52, 120.67, 40.25, and 9.77, respectively, suggesting the effect of these variables on PFOS degradation efficiency followed the sequence of Initial PFOS concentration > Current density > pH > Na<sub>2</sub>SO<sub>4</sub> concentration. The graphical 3D and 2D contour plots in Fig. 6 described the interaction of independent variables. PFOS degradation efficiency increased with the current density increasing from 10 to 50 mA/cm<sup>2</sup>, decreased from the initial PFOS concentration increasing from 10 to 90 mg/L. Higher Na<sub>2</sub>SO<sub>4</sub> concentration in the range of 0.01–0.1 M and lower pH in the range of 3–11 were more conducive to the degradation of PFOS. Fig. S2 (a and b) of SM shows the plots of internally studentized residuals versus predicted response, internally studentized residuals versus experimental runs, and predicted response versus experimental

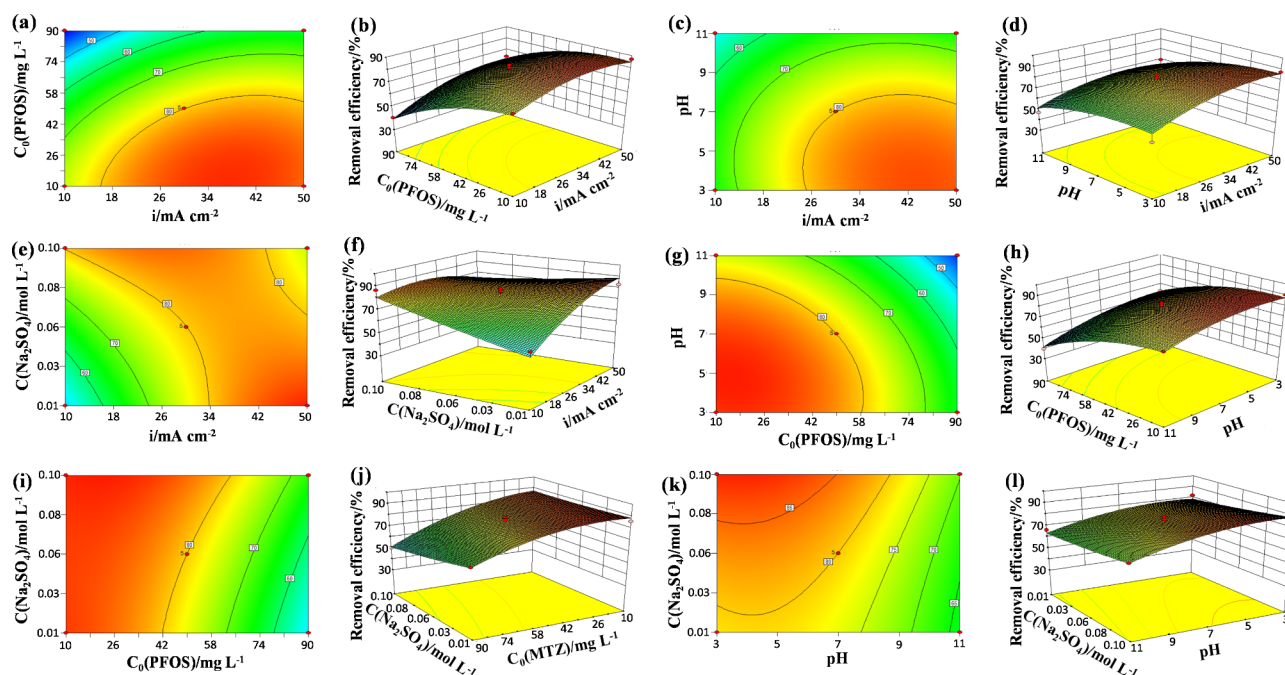


**Fig. 6** Contour and 3D response surface plots to show the interaction of different operation conditions for the PFOS degradation at Y/3DG-PbO<sub>2</sub>-15 anode

value. It can be observed from Fig. S2(a and b) that all the residuals are scattered in the standard deviation range, representing a good accordance between the experimental value and predicted response [78]. The good linear relationship between the predicted and actual values (Fig. S2(c) of SM) also confirmed the adequacy of the proposed model [79]. The optimization of electrochemical oxidation operation parameters was performed by setting the response (PFOS removal efficiency after 40 min of electrolysis, %) to maximize and setting the variables to within the working range. Table S4 of SM lists the provided solutions by the Box-Behnken methodology, the maximum PFOS degradation of 97.84% was acquired by the 42nd solution (current density=50 mA/cm<sup>2</sup>, initial PFOS concentration=12.21 mg/L, pH value=5.39, Na<sub>2</sub>SO<sub>4</sub> concentration=0.01 M). The experiment was carried out under the optimized experimental conditions to evaluate the validity of the predicted model. The obtained experimental value of 97.16% was very close to the predicted value of 97.84%.

## Conclusion

In this work, a novel Y/3DG-PbO<sub>2</sub> anode was successfully fabricated by introducing Y into the 3DG-PbO<sub>2</sub> anode. Compared with the 3DG-PbO<sub>2</sub> anode, the Y/3DG-PbO<sub>2</sub>-15 anode exhibited a denser film and smaller crystal size. At the same time, the Y/3DG-PbO<sub>2</sub>-15 anode also possessed higher oxygen evolution potential (2.04 V vs. SCE), more voltammetric quantity (0.70 C/cm<sup>2</sup> at a scan rate of 20 mV/s),

smaller charge transfer resistance (27.22 Ω/cm<sup>2</sup>), and larger •OH radical generation rate (0.155 μM/min) than those of 3DG-PbO<sub>2</sub> anode (1.96 V vs. SCE, 0.49 C/cm<sup>2</sup>, 45.31 Ω/cm<sup>2</sup> and 0.144 μM/min). As a result, the Y/3DG-PbO<sub>2</sub>-15 anode exhibited excellent electrocatalytic activity for the electrochemical degradation of PFOS. The rate constant of PFOS degradation over the Y/3DG-PbO<sub>2</sub>-15 anode was 0.045 min<sup>-1</sup>, significantly higher than 0.028 min<sup>-1</sup> over the 3DG-PbO<sub>2</sub> anode. According to the RSM, the optimum electrochemical oxidation conditions for PFOS degradation were current density=50 mA/cm<sup>2</sup>, initial PFOS concentration=12.21 mg/L, pH value=5.39, and Na<sub>2</sub>SO<sub>4</sub> concentration=0.01 M. In this case, 97.16% of PFOS removal was acquired after 40 min of electrolysis, which was very close to the predicted value of 97.84%. Both of Tafel test and consecutive electrolysis experiments confirmed the excellent stability of the Y/3DG-PbO<sub>2</sub>-15 anode. In the Tafel test, the Y/3DG-PbO<sub>2</sub>-15 electrode obtained a higher self-corrosion potential (1.360 V) and lower self-corrosion current density (0.047 A) than the 3DG-PbO<sub>2</sub> electrode (1.317 V, 0.069 A). In consecutive cycles of electrolysis, the removal percentages of PFOS over the Y/3DG-PbO<sub>2</sub>-15 anode after 20 cycles was still 97.12%, slightly lower than 99.35% of the first cycle.

## Supplementary Information

The online version contains supplementary material available at <https://doi.org/10.1186/s13065-023-01057-3>.

## Supplementary Material 1

**Author contributions**

All authors contributed to the study conception and design. Ziqi Ning, Weiwei Wang, Yitong Li, Liyue Liu and Wenqian Li prepared Materials and performed experiments. Xiaoyue Duan, Ziqi Ning, Weiwei Wang, Xuesong Zhao and Limin Chang analyzed the data and prepares figures. Weiwei Wang and Xiaoyue Duan wrote the first draft of the manuscript. All authors reviewed and approved the final manuscript.

**Funding**

This project was financially supported by the Science and Technology Project of Jilin Province, China (No. YDZJ202201ZYTS595 and No. 20230101325JC) and the National Natural Science Foundation of China (No. 52170080).

**Data Availability**

The datasets used and/or analyzed during the current study are available from the corresponding author on reasonable request.

**Declarations****Competing interests**

The authors declare no competing interests.

**Ethics approval**

Not applicable.

**Consent to participate**

Not applicable.

**Consent for publication**

Not applicable.

Received: 18 July 2023 / Accepted: 10 October 2023

**References**

1. Leung SCE, Shukla P, Chen D, Eftekhari E, An H, Zare F, Ghasemi N, Zhang D, Nguyen NT, Li Q. Emerging technologies for PFOS/PFOA degradation and removal: a review. *Sci Total Environ.* 2022;827:153669.
2. Li Z, Luo ZM, Huang Y, Wang JW, Ouyang. Recent trends in degradation strategies of PFOA/PFOS substitutes. *Chemosphere.* 2023;315:137653.
3. Sun J, Jennepalli S, Lee M, Jones A, O'Carroll DM, Manefield MJ, Bhadbhade M, Åkermark B, Das, N. Kumar. Efficient reductive defluorination of branched PFOS by metal-porphyrin complexes. *Environ Sci Technol.* 2022;56:7830–9.
4. Xu Y, Du W, Yin Y, Sun Y, Ji R, He H, Yang S, Li S, Wu J, Guo. CuO nanoparticles modify bioaccumulation of perfluorooctanoic acid in radish (*Raphanus sativus* L). *Env Pollut Bioavail.* 2022;34:34–41.
5. Xiao F. An overview of the formation of PFOA and PFOS in drinking-water and wastewater treatment processes. *J Environ Eng.* 2022;148:01822001.
6. Torres FBM, Guida Y, Weber R, Torres JPM. Brazilian overview of per- and polyfluoroalkyl substances listed as persistent organic pollutants in the Stockholm convention. *Chemosphere.* 2022;291:132674.
7. Qin W, Ren X, Zhao L, Guo L. Exposure to perfluorooctane sulfonate reduced cell viability and insulin release capacity of  $\beta$  cells. *J Environ Sci.* 2022;115:162–72.
8. Hwang JH, Sip YYL, Kim KT, Han G, Rodriguez KL, Fox DW, Afrin S, Burnstine-Townley A, Zhai L, Lee WH. Nanoparticle-embedded hydrogel synthesized electrodes for electrochemical oxidation of perfluorooctanoic acid (PFOA) and perfluorooctanesulfonic acid (PFOS). *Chemosphere.* 2022;296:134001.
9. Huang J, Wang Q, Liu S, Lai H, Tu W. Comparative chronic toxicities of PFOS and its novel alternatives on the immune system associated with intestinal microbiota dysbiosis in adult zebrafish. *J Hazard Mater.* 2022;425:127950.
10. Sun Z, Zhang C, Jiang J, Wen J, Zhou Q, Hoffmann MR. UV/Fe<sup>III</sup>NTA as a novel photoreductive system for the degradation for the degradation of perfluorooctane sulfonate (PFOS) via a photoinduced intramolecular electron transfer mechanism. *Chem Eng J.* 2022;427:130923.
11. Hearon SE, Orr AA, Moyer H, Wang M, Tamamis P, Phillips TD. Montmorillonite clay-based sorbents decrease the bioavailability of per- and polyfluoroalkyl substances (PFAS) from soil and their translocation to plants. *Environ Res.* 2022;205:112433.
12. Troitsky B, Zhu DZ, Loewen M, van Duin B, Mahmood. Nutrient processes and modeling in urban stormwater ponds and constructed wetlands. *Can Water Resour J.* 2019;44:230–47.
13. Gorito AM, Ribeiro AR, Gomes CR, Almeida CMR, Silva AMT. Constructed wetland microcosms for the removal of organic micropollutants from freshwater aquaculture effluents. *Sci Total Environ.* 2018;644:1171–80.
14. Samuel MS, Shang M, Niu J. Photocatalytic degradation of perfluoroalkyl substances in water by using a duo-functional tri-metallic-oxide hybrid catalyst. *Chemosphere.* 2022;293:133568.
15. Maza WA, Breslin VM, Feygelson TI, DeSario PA, Pate BB, Owrutsky JC, A.Epshteyn. Degradation of perfluorooctanesulfonate (PFOS) by sub-band-gap irradiation of hydrogen-terminated nanodiamond. *Appl Catal B: Environ.* 2023;325:122306.
16. Yang B, Wang J, Jiang C, Li J, Yu G, Deng S, Lu S, Zhang P, Zhu C. Zhuo. Electrochemical mineralization of perfluorooctane sulfonate by novel F and sb co-doped Ti/SnO<sub>2</sub> electrode containing Sn-Sb interlayer. *Chem Eng J.* 2017;316:296–304.
17. Rodriguez-Freire L, Balachandran R, Sierra-Alvarez R, Keswani M. Effect of sound frequency and initial concentration on the sonochemical degradation of perfluorooctane sulfonate (PFOS). *J Hazard Mater.* 2015;300:662–9.
18. Wu B, Hao S, Choi Y, Higgins CP, Deeb R, Strathmann TJ. Rapid destruction and defluorination of perfluorooctanesulfonate by alkaline hydrothermal reaction. *Environ Sci Technol Lett.* 2019;6:630–6.
19. Singh RK, Fernando S, Baygi SF, Multari N, Thagard SM, Holsen TM. Breakdown products from perfluorinated alkyl substances (PFAS) degradation in a plasma-based water treatment process. *Environ Sci Technol.* 2019;53:2731–8.
20. Kim TH, Lee SH, Kim HY, Doudrick K, Yu S, Kim SD. Decomposition of perfluorooctane sulfonate (PFOS) using a hybrid process with electron beam and chemical oxidation. *Chem Eng J.* 2019;361:1363–70.
21. Zhou Q, Liu D, Yuan G, Tang Y, Cui K, Jiang S, Xia Y, Xiong W. Efficient degradation of phenolic wastewaters by a novel by a novel Ti/PbO<sub>2</sub>-Cr-PEDOT electrode with enhanced electrocatalytic activity and chemical stability. *Sep Purif Technol.* 2022;281:119735.
22. Fu X, Han Y, Xu H, Su Z, Liu L. Electrochemical study of a novel high-efficiency PbO<sub>2</sub> anode based on a cerium-graphene oxide co-doping strategy: Electrodeposition mechanism, parameter optimization, and degradation pathways. *J Hazard Mater.* 2022;422:126890.
23. Shi H, Wang Y, Li C, Pierce R, Gao S, Huang Q. Degradation of perfluorooctanesulfonate by reactive electrochemical membrane composed of magneli phase titanium suboxide. *Environ Sci Technol.* 2019;53:14528–37.
24. Li C, Wang Y, Wang Y, Wang Z, Huang Q. Electrochemical oxidation combined with UV irradiation for synergistic removal of perfluorooctane sulfonate (PFOS) in water. *J Hazard Mater.* 2022;436:129091.
25. Trzcinski AP, Harada K. Adsorption of PFOS onto graphite intercalated compound and analysis of degradation by-products during electro-chemical oxidation. *Chemosphere.* 2023;323:138268.
26. Le TXH, Haflich H, Shah AD, Chaplin BP. Energy-efficient electrochemical oxidation of perfluoroalkyl substances using a Ti<sub>4</sub>O<sub>7</sub> reactive electrochemical membrane anode. *Environ Sci Technol Lett.* 2019;6:504–10.
27. Zhang Z, Xiao Q, Du X, Xue T, Yan Z, Liu Z, Zhang H, Qi T. The fabrication of Ti<sub>4</sub>O<sub>7</sub> particle composited modified PbO<sub>2</sub> coating electrode and its application in the electrochemical oxidation degradation of organic wastewater. *J Alloy Compd.* 2022;897:162742.
28. Wang X, Wang L, Wu D, Yuan D, Ge H. Wu. PbO<sub>2</sub> materials for electrochemical environmental engineering: a review on synthesis and applications. *Sci Total Environ.* 2023;855:158880.
29. Dolatabadi M, Ehrampoush MH, Pournamdari M, Ebrahimi AA, Fallahzadeh H, Ahmadzadeh S. Simultaneous electrochemical degradation of pesticides from the aqueous environment using Ti/SnO<sub>2</sub>-Sb<sub>2</sub>O<sub>3</sub>/PbO<sub>2</sub>/Bi electrode; process modeling and mechanism insight. *Chemosphere.* 2023;311:137001.
30. Duan X, Wang W, Wang Q, Sui X, Li N, Chang L. Electrochemical degradation of perfluorooctane sulfonate (PFOS) on a 3D graphene-lead dioxide (3DG-PbO<sub>2</sub>) composite anode: Electrode characterization, degradation mechanism and toxicity. *Chemosphere.* 2020;260:127587.
31. Chen S, Liu P, Li Y, Zhu M, Dang Y, Zhou Y. Engineering the doping amount of rare earth element erbium in CdWO<sub>4</sub>: influence on the electrochemical

- performance and the application to the electrochemical detection of bisphenol A. *Electroanal Chem.* 2022;904:115867.
32. Wang Q, Fan H, Xiao Y, Zhang Y. Applications and recent advances of rare earth in solid oxide fuel cells. *J Rare Earth.* 2022;40:1668–81.
  33. Lyu WY, Liu WD, Li M, Hong M, Guo K, Luo J, Xing J, Sun Q, Xu S, Zou J, Chen ZG. The effect of rare earth element doping on thermoelectric properties of GeTe. *Chem Eng J.* 2022;446:137278.
  34. Jin Y, Wang F, Xu M, Hun Y, Fang W, Wei Y, Zhu C. Preparation and characterization of Ce and PVP co-doped PbO<sub>2</sub> electrode for waste water treatment. *J Taiwan Inst Chem E.* 2015;51:135–42.
  35. Zhang Y, He P, Zhou L, Dong F, Yang D, Lei H, Du L, Jia L, Zhou. Optimized terbium doped Ti/PbO<sub>2</sub> dimensional stable anode as a strong tool for electrocatalytic degradation of imidacloprid waste water. *Ecotox Environ Safe.* 2020;188:109921.
  36. Lan H, Tao Q, Ma N, Chen L, Wei L, Weng M, Dai Q. Electrochemical oxidation of lamivudine using graphene oxide and Yb co-modified PbO<sub>2</sub> electrodes: characterization, influence factors and degradation mechanisms. *Sep Purif Technol.* 2022;301:121856.
  37. Wang K, Xing X, Liu W, Jiang Y, Li H, Lu Y, Chen H. Fabrication of a novel PbO<sub>2</sub> electrode with rare earth elements doping for p-nitrophenol degradation. *J Environ Chem Eng.* 2023;11:109513.
  38. Zhang Z, Yi G, Li P, Wang X, Wang X, Zhang C, Zhang Y, Sun Q. Electrochemical oxidation of hydroquinone using Eu-doped PbO<sub>2</sub> electrodes: Electrode characterization, influencing factors and degradation pathways. *Electroanal Chem.* 2021;895:115493.
  39. Reddy IN, Reddy CV, Cho M, Kim D, Shim. Cu<sup>2+</sup> and Y<sup>3+</sup> co-doped effect on morphology, structural, optical and photoelectrochemical properties of Fe<sub>2</sub>O<sub>3</sub> photoanode. *Electroanal Chem.* 2020;878:114692.
  40. Hou L, Xia L, Zhou R, Li J, Li R, Zhao Z, Yuan G, Duan A. Effect of yttrium on catalytic performance of Y-doped TiO<sub>2</sub> catalysts for propane dehydrogenation. *J Rare Earth.* In press.
  41. Ghafoor A, Bibi I, Majid F, Ata S, Nouren S, Raza Q, Mansoor S, Alqahtani FO, Elqahtani ZM, Mehr-un-Nisa, M. Iqbal. Yttrium and cobalt doped LaNiO<sub>3</sub> nanoparticles synthesis and solar light driven photocatalytic removal of rhodamine B. *Mater Res Bull.* 2023;159:112112.
  42. Wei Y, Wang L, Chen C. Yttrium doping enhances the photoelectrochemical water splitting performance of ZnO nanorod array films. *J Alloy Compd.* 2022;896:163144.
  43. Yu S, Hao C, Li Z, Zhang R, Dang Y, Zhu JJ. Promoting the electrocatalytic performance of PbO<sub>2</sub> nanocrystals via incorporation of Y<sub>2</sub>O<sub>3</sub> nanoparticles: degradation application and electrocatalytic mechanism. *Electrochim Acta.* 2021;369:137671.
  44. Khalfaouy RE, Turan S, Rodriguez MA, Dermenci KB, Savaci U, Addaou A, Laajeb A. Lahsini. Solution combustion synthesis and electrochemical properties of yttrium-doped LiMnPO<sub>4</sub>/C cathode materials for lithium ion batteries. *J Rare Earth.* 2020;38:976–82.
  45. Muruganandam S, Kannan S, Anishia SR, Krishnan P. Electrochemical performance of Yttrium doped SnO<sub>2</sub>-NiO nanocomposite for energy storage applications. *J Phys Chem Solids.* 2023;179:111420.
  46. Du Y, Zhang X, Shi Y, Hou X, Li F, Zhang Q, Tai Q, Liu P, Zhao XZ. Optimized crystallization and defect passivation with Yttrium (III) doped MAPbBr<sub>3</sub> film for highly efficient and stable hole-transport-layer-free carbon-based perovskite solar cells. *J Alloy Compd.* 2021;890:161909.
  47. Li M, Huan Y, Yan X, Kang Z, Guo Y, Li Y, Liao X, Zhang R, Zhang Y. Efficient yttrium(III) chloride-treated TiO<sub>2</sub> electron transfer layers for performance-improved and hysteresis-less perovskite solar cells. *ChemSusChem.* 11 (2018)171 – 177.
  48. Wang Y, Li L, Wang Y, Shi H, Wang L, Huang Q. Electrooxidation of perfluorooctanesulfonic acid on porous Magnéli phase titanium suboxide anodes: impact of porous structure and composition. *Chem Eng J.* 2022;431:133929.
  49. Wu W, Huang ZH, Lim TT. Recent development of mixed metal oxide anodes for electrochemical oxidation of organic pollutants in water. *Appl Catal A: Gen.* 2014;480:58–78.
  50. Bibin J, Mohan M, Dhanyaprabha KC, Hysen T. NiCo<sub>2</sub>O<sub>4</sub> nanoparticles anchored on reduced graphene oxide with enhanced catalytic activity towards the reduction of p-Nitrophenol in water. *Colloid Surf A.* 2022;643:128717.
  51. Sun Y, Zhang C, Rong H, Wu L, Lian B, Wang Y, Chen Y, Tu Y, Waite DT. Electrochemical Ni-EDTA degradation and ni removal from electroless plating wastewaters using an innovative Ni-doped PbO<sub>2</sub> anode: optimization and mechanism. *J Hazard Mater.* 2022;424:127655.
  52. Shen Y, Li Y, He Y, Zhang C, Xie C, Zhang H, Han E. Preparation of high performance superhydrophobic PVDF-PbO<sub>2</sub>-ZrO<sub>2</sub> composite electrode and its application in the degradation of Paracetamol and industrial oily wastewater. *Electroanal Chem.* 2022;911:116231.
  53. Xu P, He X, Mao J, Tang Y. Fabrication of Ti/SnO<sub>2</sub>-Sb/Ce-PbO<sub>2</sub> anode from methanesulfonate bath and its electrocatalytic activity. *J Electrochem Soc.* 2019;166:638–44.
  54. Ma X, He C, Yan Y, Chen J, Feng H, Hu J, Zhu H, Xia Y. Energy-efficient electrochemical degradation of ciprofloxacin by a Ti-foam/PbO<sub>2</sub>-GN composite electrode: electrode characteristics, parameter optimization, and reaction mechanism. *Chemosphere.* 2023;315:137739.
  55. Pan Y, Luo Y, Li C, Wang R, Yuan Y, Li M, Na P. Preparation and characterization of Ti/SnO<sub>2</sub>-Sb<sub>2</sub>O<sub>3</sub>/α-PbO<sub>2</sub>/Ce-Nd-β-PbO<sub>2</sub> composite electrode for methyl orange degradation. *J Solid State Electr.* 2020;24:545–55.
  56. Yan Y, Ma X, Xia Y, Feng H, Liu S, He C, Ding Y. Mechanism of highly efficient electrochemical degradation of antibiotic sulfadiazine using a layer-by-layer GNPs/PbO<sub>2</sub> electrode. *Environ Res.* 2023;217:114778.
  57. Yanagi G, Furukawa M, Tateishi I, Katsumata H, Kaneco S. Electrochemical decolorization of methylene blue in solution with metal doped Ti/α, β-PbO<sub>2</sub> mesh electrode. *Sep Sci Technol.* 2021;57:325–37.
  58. Wang SW, He ZH, Chen JG, Yang SY, Wei YY, Wang K, Wang W, Ma X, Liu ZT. Cobalt-yttrium bimetal catalyzed hydrogenolysis of aryl ethers. *Biomass Bioenerg.* 2022;164:106565.
  59. Liu Y, Zhu W, Chen Z, Yu Q, Hu Q, Zheng Z, Gui L, Song Y. Preparation of cobalt-manganese-modified lead dioxide anodes and the study of their electrochemical performance in electrowinning copper. *Int J Hydrogen Energ.* 2021;46:6380–94.
  60. Xia Y, Bian X, Xia Y, Zhou W, Wang L, Fan S, Xiong P, Zhan T, Dai Q, Chen J. Effect of indium doping on the PbO<sub>2</sub> electrode for enhanced electrochemical oxidation of aspirin: an electrode comparative study. *Sep Purif Technol.* 2020;237:116321–7.
  61. Seekaew Y, Wisitsoraat A, Phokharatkul D, Wongchoosuk C. Room temperature toluene gas sensor based on TiO<sub>2</sub> nanoparticles decorated 3D graphene-carbon nanotube nanostructures. *Sens Actuat B: Chem.* 2019;279:69–78.
  62. Wei F, Liao D, Lin Y, Hu C, Ju J, Chen Y, Feng D. Electrochemical degradation of reverse osmosis concentrate (ROC) using the electrodeposited Ti/TiO<sub>2</sub>-NTs/PbO<sub>2</sub> electrode. *Sep Purif Technol.* 2021;258:118056.
  63. Yu L, Xue J, Zhang L, Tang C, Guo Y. Fabrication of a stable Ti/Pb-TiO<sub>2</sub>NWs/PbO<sub>2</sub> anode and its application in benzoquinone degradation. *Electrochim Acta.* 2021;368:137532.
  64. Wu L, Zhang C, Sun Y, Wang Y, Lian B, Chen Y, Tu Y, Waite TD. Cu-mediated optimization of PbO<sub>2</sub> anodes for electrochemical treatment of electroless nickel plating wastewater. *Chem Eng J.* 2022;450:138188.
  65. Xia Y, Feng J, Fan S, Zhou W, Dai Q. Fabrication of a multi-layer CNT-PbO<sub>2</sub> anode for the degradation of isoniazid: kinetics and mechanism. *Chemosphere.* 2021;263:128069.
  66. Liu J, Liu F, Xu J, Han Z. Effect of current density on interface structure and performance of CF/β-PbO<sub>2</sub> electrodes during zinc electrowinning. *Ceram Int.* 2020;46:2403–8.
  67. Man S, Ge X, Xu K, Yang H, Bao H, Sun Q, He M. Fabrication of a Ti/PbO<sub>2</sub> electrode with Sb doped SnO<sub>2</sub> nanoflowers as the middle layer for the degradation of methylene blue, norfloxacin and p-dihydroxybenzene. *Sep Purif Technol.* 2022;280:119816.
  68. Lu Z, Liu L, Gao W, Zhai Z, Song H, Chen B, Zheng Z, Yang B, Geng C, Liang J, Jiang X, Huang N. Manufacturing 3D nano-porous architecture for boron-doped diamond film to efficient abatement of organic pollutant: synergistic effect of hydroxyl radical and sulfate radical. *Sep Purif Technol.* 2022;302:122080.
  69. Rathinavelu S, Divyapriya G, Joseph A, Nambi IM, Muthukrishnan AB, Jayaraman G. Inactivation behavior and intracellular changes in *Escherichia coli* during electro-oxidation process using Ti/Sb-SnO<sub>2</sub>/PbO<sub>2</sub> anode: elucidation of the disinfection mechanism. *Environ Res.* 2022;210:112749.
  70. Cong Y, Wu Z. Electrocatalytic generation of radical intermediates over lead dioxide electrode doped with fluoride. *J Phys Chem.* 2007;111:3442–6.
  71. Yao Y, Teng G, Yang Y, Ren B, Cui L. Electrochemical degradation of Neutral red on PbO<sub>2</sub>/α-Al<sub>2</sub>O<sub>3</sub> composite electrodes: Electrode characterization, byproducts and degradation mechanism. *Sep Purif Technol.* 2019;227:115684.
  72. Zhuo Q, Luo M, Guo Q, Yu G, Deng S, Xu Z, Yang B, Liang. Electrochemical oxidation of environmentally persistent perfluorooctane sulfonate by a novel lead dioxide anode. *Electrochim Acta.* 2016;213:358–67.

73. Zhuo Q, Han J, Niu J, Zhang J. Degradation of a persistent organic pollutant perfluorooctane sulphonate with Ti/SnO<sub>2</sub>-Sb<sub>2</sub>O<sub>5</sub>/PbO<sub>2</sub>-PTFE anode. *Emerg Contam.* 2020;6:44–52.
74. Dong G, Lang K, Gao Y, Zhang W, Guo D, Li J, Chai DF, Jing L, Zhang Z, Wang Y. A novel composite anode via immobilizing of Ce-doped PbO<sub>2</sub> on CoTiO<sub>3</sub> for efficiently electrocatalytic degradation of dye. *J Colloid Interf Sci.* 2022;608:2921–31.
75. Yu X, Dang X, Li S, Meng X, Hou H, Wang P, Wang Q. Abatement of chlorobenzene by plasma catalysis: parameters optimization through response surface methodology (RSM), degradation mechanism and PCDD/Fs formation. *Chemosphere.* 2022;298:134274.
76. Wu Y, Kong LH, Shen RF, Guo XJ, Ge WT, Zhang WJ, Dong ZY, Yang X, Chen Y, Lang WZ. Highly dispersed and stable Fe species supported on active carbon for enhanced degradation of rhodamine B through peroxymonosulfate activation: mechanism analysis, response surface modeling and kinetic study. *J Environ Chem Eng.* 2022;10:107463.
77. Abidi J, Clematis D, Samet Y, Delucchi M, Cademartori D, Panizza M. Influence of anode material and chlorides in the new-gen solid polymer electrolyte cell for electrochemical oxidation – optimization of Chloroxylenol degradation with response surface methodology. *Electroanal Chem.* 2022;920:116584.
78. Murshed MK, Dursun AY, Dursun G. Application of response surface methodology on photocatalytic degradation of Astrazon Orange G dye by ZnO photocatalyst: internal mass transfer effects. *Chem Eng Res Des.* 2022;188:27–38.
79. Samarghandi MR, Ansari A, Dargahi A, Shabanloo A, Nematollahi D, Khazaei M, Nasab HZ, Vaziri Y. Enhanced electrocatalytic degradation of bisphenol A by graphite/β-PbO<sub>2</sub> anode in a three-dimensional electrochemical reactor. *J Environ Chem Eng.* 2021;9:106072.

### Publisher's Note

Springer Nature remains neutral with regard to jurisdictional claims in published maps and institutional affiliations.